Article

A Comparative Study on Ag-Doped and Surfactant Assisted MnO₂ Prepared by Direct and Pulse Current Electrodeposition on Surgical Grade Stainless Steel as High-Performance Supercapacitor

Mohammad Faridi,[a] Alireza Nari,[a,b] Hamideh Kalhor*,[c] and Mohammad H. Dadjoo[b,d]

[a]*Department of Chemistry, Amirkabir University of Technology (Tehran Polytechnic), Tehran, Iran*

[b]*Research and Development Center, Atlas Energy Co. Atlas Tajhiz Mandegar Corporation, Tehran, Iran*

[c]*Department of Chemistry, Faculty of Sciences, Tarbiat Modares University, Tehran, Iran*

[d]*Department of Chemical Engineering, Amirkabir University of Technology (Tehran Polytechnic), Tehran, Iran*

Direct and pulse current electrodeposition techniques were applied for preparation of novel electro-active manganese oxides. The influences of Ag doping and addition of cetyltrimethylammonium bromide (CTAB) on electrochemical properties were discussed. The morphology and structure of the electrodes are studied by different techniques including field emission scanning electron microscopy (FE-SEM), contact angle and X-ray photoelectron spectroscopy (XPS). Electrochemical behavior of the samples are investigated by cyclic voltammetry (CV), constant current charge-discharge (CC), and electrochemical impedance spectroscopy (EIS). The specific capacitances were measured to be 269, 315, 435, 442, 480 and 508 F g⁻¹ for M-g, M-p, MC-g, MC-p, MCA-g and MCA-p (current density = 1 A g⁻¹), respectively. The MCA-p exhibit high specific capacitance, excellent cycling stability (only 7.5% loss after 1000 cycles at 1 A g⁻¹), and high energy densities (71 Wh kg⁻¹). Ag doping and addition of CTAB which provides more active sites for the pseudocapacitive reactions.

Keywords: supercapacitor, MnO₂, CTAB, Ag doping, pulsed current

Introduction

Research on electrochemical capacitors (ECs) has generated growing attention from both academia and industry in recent years, with efforts focused on developing safe, stable, high energy/power density, and low cost materials.[1] ECs are considered a promising power storage device for backup power storage, peak power sources and hybrid electric and fuel cell vehicles. Based on the intrinsic principles of charge storage and discharge in ECs, the energy stored is either capacitive (non-faradaic) or pseudocapacitive (faradaic) *in nature*. The non-faradaic process relies on charge separation at the interface between the electrode and the ionic solution giving rise to an electrical double layer, whereas the faradaic process consists of redox reactions occurring within the active electrode materials.[2-4]

Transition metal oxides have been appropriate active materials for ECs. Various transition metal oxides, such as RuO_2,[5,6] Co_3O_4,[7] NiO,[8,9] Fe_2O_3,[10] SnO_2,[11] MnO_2,[12-15] and etc., are being considered for the supercapacitor applications with their charge storage mechanisms based on pseudocapacitance. In recent years, manganese dioxide (MnO_2) can be used as an active electrode materials in ECs. The capacitance of MnO_2 electrode is believed to be predominant due to pseudocapacitance, which is attributed to reversible redox transitions involving exchange of protons and/or cations with the electrolyte.[16] The methods used for the fabrication of manganese oxide electrodes are mostly based on the deposition of thin films or pasting manganese oxide powders mixed with binders and conductive additives on conductive current collectors.

Since electrochemical deposition is clean, controllable and uncomplicated method, many investigations have been focused on the electrochemical deposition of manganese dioxide films. Electrochemical deposition has various methods, such as galvanostatic,[17] potentiostatic,[18]

*e-mail: kalhor1363.h@gmail.com

potentiodynamic,[19] and pulse deposition.[20] For having uniform deposition it is necessary to have constant current density during deposition. In addition, pulse deposition as one of essential techniques has been useful to synthesize different thin films. It can improve chemical-physical properties of active materials.[21,22] For a manganese oxide supercapacitor, the oxide film can be deposited on many substrates, which act as current collectors. Along with graphite,[23] nickel[24] and other conductive materials,[25] stainless steel can be used because it is inert in various supercapacitor electrolytes. Among the various grades of stainless steel, Surgical Grade Stainless Steel (316L) are particularly attractive because of nonmagnetic properties as well as good strength and corrosion resistance in such electrolytes as KOH, Na_2SO_4 solutions and others.

The electrochemical performance of supercapacitors were improved by adding a surfactant agent.[26-29] The researchers prepared polythiophenes (PTs) by chemical oxidative polymerization in presence and absence of three different surfactants (cationic-cetyltrimethylammonium bromide (CTAB), anionic-sodium dodecyl sulfate (SDS) and non-ionic-Triton X-100) using $FeCl_3$ as oxidant. The PT prepared with Triton X-100 exhibited higher specific capacitance of 117 F g^{-1} compared to 78 F g^{-1} of surfactant free PT by the cyclic voltammetry test.[30] Wu and Wang[31] prepared nickel oxide film with open macropores by anodic deposition in the presence of surfactant CTAB and it shows a very high capacitance of 1110 F g^{-1} at scan rate of 10 mV s^{-1}. The influencing mechanism of the surfactant concentrations has not been fully understood.[31] It is important Ag-doping in supercapacitor fabrication. Ag-doped RuO_2 showed much higher specific capacitance compared to undoped RuO_2.[32] Huang *et al.*[33] prepared the array of CuO nanosheet and it is doped by Ag via the silver mirror reaction. The specific capacitance of the Ag-doped CuO nanosheet electrode is 689 F g^{-1}, much higher than that of the unmodified CuO nanosheet arrays (418 F g^{-1}).

In this work, the manganese oxide films were electrodeposited by the direct galvanostatic and pulse current methods from potassium permanganate electrolyte, respectively. In addition, we doped Ag into electrode based on MnO_2 to improve charge transfer resistance. A surface-active molecule with a polar group were also used for preparation of supercapacitor electrodes. Thus, MnO_2 was electrodeposited in presence of CTAB and $AgNO_3$ with both pulse current and direct galvanostatic methods. The characteristics of MnO_2 active materials were investigated by field emission scanning electron microscope (FE-SEM), X-ray photoelectron spectroscopy (XPS), contact angle, constant current charge-discharge (CC), electrochemical impedance spectroscopy (EIS) and cyclic voltammetry (CV).

Experimental

Potassium permanganate ($KMnO_4$), silver nitrate ($AgNO_3$) and cetyltrimethylammonium bromide (CTAB) were applied for electrodeposition. All of materials were purchased from the Merck Company (Germany). All solutions were prepared using deionized water and stainless steel (316 grade) 1 mm thickness electrodes used as substrate.

A 1 cm^2 stainless steel slice was taken as anode electrode. At first, it was burnished with rough sand paper. Then, it was etched for 5 min in 0.5 mol L^{-1} NaOH aqueous solution by ultrasonic bath. After that it was rinsed with ethanol and deionized water, respectively.

The direct and pulse current electrodeposition were performed in a two-electrode system using the stainless steel substrate as a working electrode and a platinum counter electrode from 10 mol L^{-1} $KMnO_4$ containing 0 and 2 mol L^{-1} $AgNO_3$ at ambient temperature. The direct galvanostatic electrodeposition has carried out at current density of 2 mA cm^{-2} for 60 seconds and pulse current deposition performed at the same current density for 240 deposition cycles with on-time of 0.25 s and off-time of 0.5 s. The CTAB in concentration 1 mol L^{-1} was added to predetermined solutions to investigate surface morphology of samples and its effects on electrochemical behavior of electrodes. Stainless steel electrodes was weighed after electrodeposition and subtract of primary mass of electrode before electrodeposition to obtain mass of active materials. Table 1 shows composition of manganese oxide base of electrodes.

X-ray photoelectron spectroscopy (XPS) has been measured with a Kratos XSAM 800 ultrahigh vacuum photoelectron spectrometer using the Mg Kα line as the excitation source. The microstructure and morphology of MnO_2 were investigated by means of field-emission scanning electron microscopy (Carl ZEISS-SIGMA VP, Germany). Surface wettability was evaluated by water angle contact measurement, using a commercial contact angle meter (Dataphysics OCA15plus, Germany). The water drops (1 mL, ultra-pure) put onto the film surface using vertical syringe.

The electrochemical techniques such as CV, CC and EIS were used to study the capacitance of the modified working electrodes. Platinum grid (1 cm^2) and saturated Ag/AgCl were used as counter and reference electrodes, respectively. In these techniques a solution of 1 mol L^{-1} sodium sulfate (Na_2SO_4) was used as supporting electrolyte. First of all, CV-grams were carried out in the range of 0.0 to 0.9 V at various scan rate (2-50 mV s^{-1}). The galvanostatic charge-discharge cycling between 0 and 1 V

Table 1. Composition of manganese oxide based of electrodes

Abbreviation	[KMnO$_4$] / (mol L^{-1})	[CTAB] / (mol L^{-1})	[AgNO$_3$] / (mol L^{-1})	Method of electrodeposition
M-g	10	–	–	
MC-g	10	1	–	galvanostatic
MCA-g	10	1	2	
M-p	10	–	–	
MC-p	10	1	–	pulse current
MCA-p	10	1	2	

CTAB: cetyltrimethylammonium bromide.

of the samples in different current densities (1-8 A g^{-1}) were studied. Furthermore EIS measurements have been carried out at frequency range of 10 kHz to 10 mHz. All of the electrochemical tests were performed by using a ZIVE SP1 potentiostat/galvanostat/FRA workstation (WonATech, Korea).

Specific capacitance (C_S) in F g^{-1} were calculated through galvanostatic charge-discharge measurements using the following equation:

$$C_S = \frac{I \, \Delta t}{\Delta V} \tag{1}$$

where I is the discharge current density in A g^{-1}, Δt is the discharge duration in s, and ΔV is the potential range in V. Energy density (ED) in Wh kg^{-1} derived from the galvanostatic discharge curves using the following equation:

$$ED = \frac{C_S \, \Delta V^2}{2 \times 3600} \tag{2}$$

where C_S is the specific capacitance in F g^{-1} and ΔV is the potential range in V.

Results and Discussion

### Morphological and structural characterization

Figure 1 presents FE-SEM images of samples, which show very different morphology. The formation of oxygen-containing intermediate Mn^{III} species (e.g., MnOOH, [Mn(H$_2$O)$_6$]$^{3+}$, and Mn$_2$O$_3$) and the growth of passive layers on the anode surface were the main reasons for the difference in the morphology of samples. In pulse current deposition, during t$_{off}$, dissolution and/or removal of the passive intermediate species took place on the anode surface. Therefore, new and/or fresh sites were created after each off-time, and grain growth prevailed at the next on-time. In other words, the nucleation rate decreased, so the formation of larger grains was possible.[34] Consequently, as seen in

Figures 1b, 1d and 1f, pulse current deposited MnO$_2$ are relatively compact and well covered with spherical grains of uniform size. The results reveal that pulse current deposition causes the morphology of MnO$_2$ to be more ordinary and more compact (Figures 1b, 1d and 1f). Furthermore, micrographs clearly illustrate that the Ag addition significantly affect the appearance of the oxide electrodes. In the presence of CTAB, agglomerated oxide nanoparticles with a foam-like structure were observed (Figure 1a). In contrast, without structure-directing surfactants, denser film structures were observed (Figures 1c-f). Surfactants significantly affect the morphology of the MnO$_2$ films. They play an important role in the nucleation and growth of hybrid films through the hemisphere-micelle formation at the electrode-liquid interface.[35]

Morphological results presented in Figure 2 are further studied by performing contact angle measurement. Contact angle of 0° means complete wetting, and contact angle of 180° corresponds to complete non-wetting. The contact angles were found to be 72, 63, 66 and 39° for MC-g, MC-p, MCA-g and MCA-p, respectively. Contact angle of MC-p and MCA-p is clearly lower than that of MC-g and MCA-g indicating better wettability of pulse method synthesized electrodes. These results recognized that MC-p and MCA-p had more hydrophilic groups. In addition, these results show that with Ag doping the contact angle decreases and finally film surface becomes more hydrophilic. Generally, low water contact angle increases the electrochemical performance, where interfacial contact at electrolyte-electrode is important.[36]

XPS test provides a sensitive measurement of a chemical state in near surface region of material. To obtain information on surface chemical states of the working electrodes, XPS analysis was performed (Figure 3). In Figures 3a and 3b, the spectrums have been smoothed using 9-point Savitzky-Golay filtering.[37] The O1s peak region can be deconvoluted into two components: (*i*) Mn−O−Mn with binding energy (BE) ca. 529 eV; and (*ii*) Mn−O−H with BE ca. 533 eV (Figures 3a and 3b). The Mn2p spectra of these samples are quite similar and all exhibit multiple
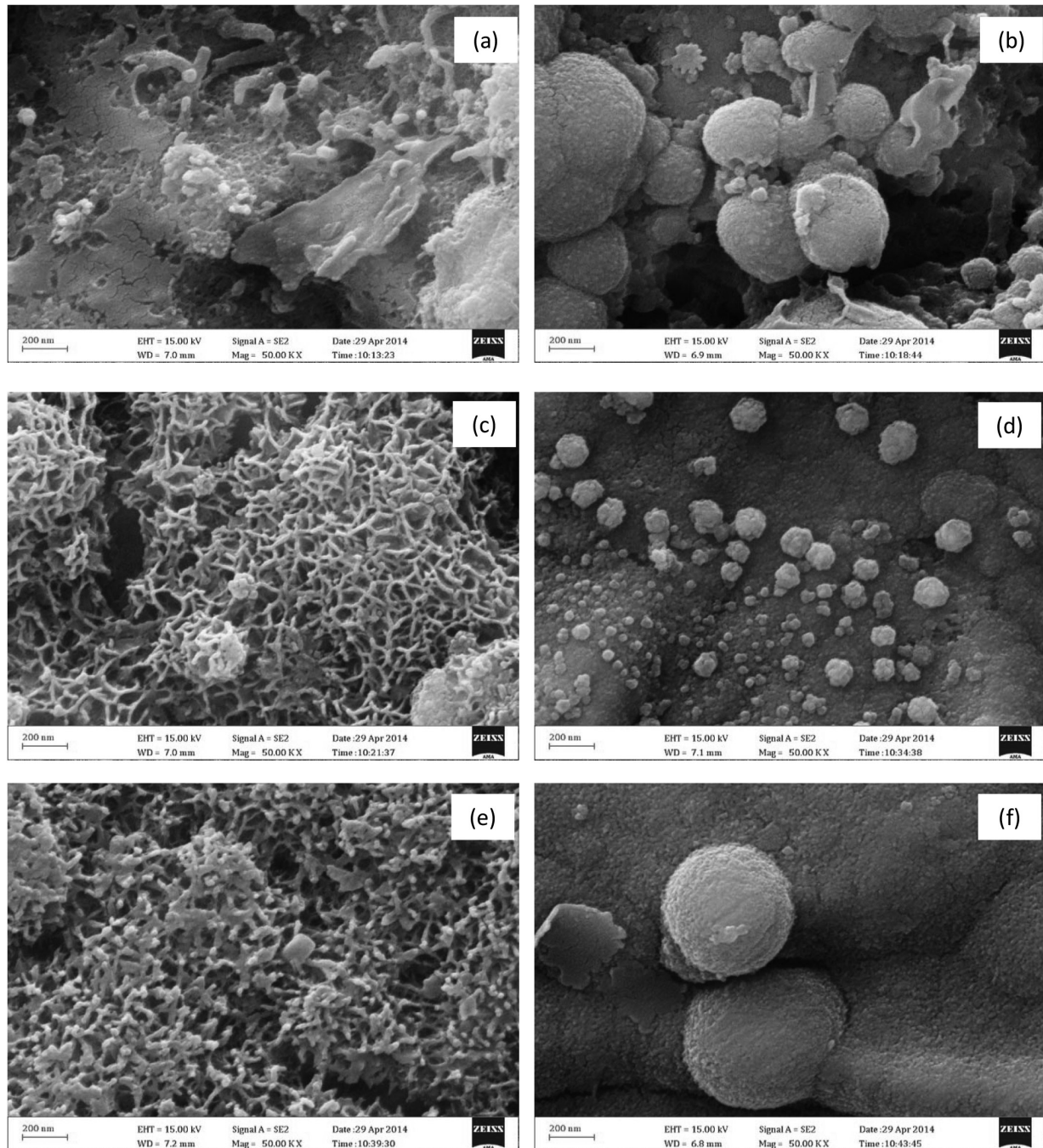
Figure 1. FE-SEM images of (a) M-g; (b) M-p; (c) MC-g; (d) MC-p; (e) MCA-g; (f) MCA-p.

splitting with two main peaks located at 642.2 and 664.0 eV, which can be assigned to $Mn2p_{3/2}$ and $Mn2p_{1/2}$ of Mn^{4+} in MnO_2, respectively (Figures 3c and 3d). Binding energy of $Ag3d_{5/2}$ peak is near 367.9 eV for MCS-p, suggesting that silver element exists as the form of Ag^+ ions (Figure 3e) that indicating to $AgMnO_2$.[38] The Mn2p spectra of $AgMnO_2$ was individually divided by curve fitting to obtain the ionic state information of the element and to estimate the relative proportion of the different ionic states.[39] As a result, the content of Mn^{III} is higher than the others and

the negative charge is more on MCA-p. Therefore, more Ag^+ ions can be absorbed and more Ag nanoparticles are doped on MCA-p.

Electrochemical characterization

MnO_2 electrodes were subjected to CV in 0.5 mol L^{-1} Na_2SO_4 and they were found to exhibit capacitance behavior. Figure 4 shows the CV curves of the MnO_2 films at various scan rates (2-50 mV s^{-1}). The rectangular shapes
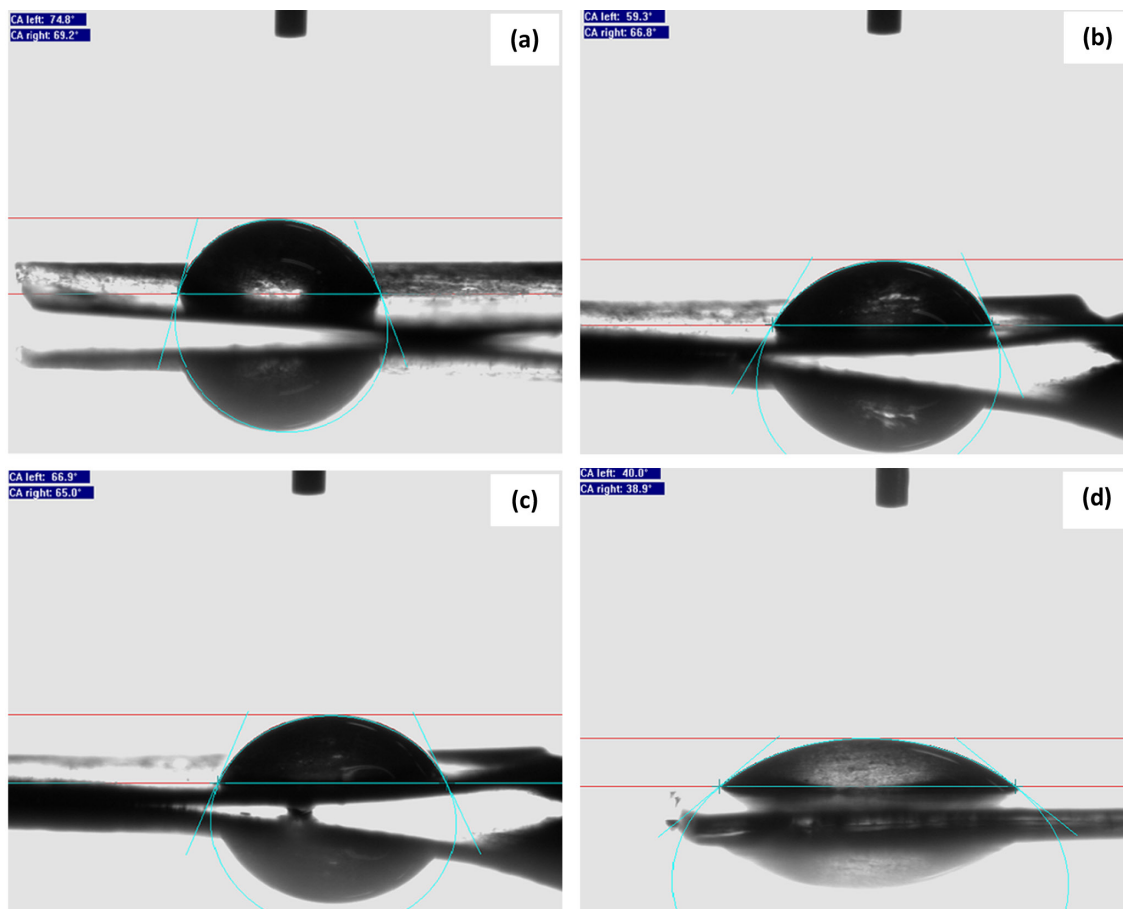
Figure 2. Measurement of water contact angle on the surface of (a) MC-g; (b) MC-p; (c) MCA-g; (d) MCA-p.

and mirror-image characteristics of the CV curves reveal the ideal pseudocapacitive behavior of all electrodes. The main information of Figures 5a-f is stated as follows: (*i*) the films prepared with pulsed current method have higher capacitances than that of the films electrodeposited by galvanostatic direct, due to their morphologies that lead to better diffusion of electrolyte ions; (*ii*) the electrochemical capacitance of MnO$_2$ can be improved in the presence of CTAB and AgNO$_3$; (*iii*) the MCA-p film have the largest area of cyclic voltammograms in higher scan rate (50 mV s^{-1}), which means that this film has the best high power rate capacitance; (*iv*) the films were prepared with pulsed current method have the best ideally cyclic voltammograms from higher to lower scan rate, indicating that these films have best charge and discharge efficiency.[40] Specific capacitances of all MnO$_2$ based films at different scan rates are calculated (Supplementary Information section, Table S1). The specific capacitances were measured to be 264, 319, 425, 462, 465 and 516 F g^{-1} at 2 mV s^{-1} for M-g, M-p, MC-g, MC-p, MCA-g and MCA-p, respectively. These data indicate that the C$_S$ increase by doping of Ag into MnO$_2$ based electrodes for both methods of synthesis. This can be explained from, improved conductivity of

electrodes by introducing the Ag in MCA-g and MCA-p samples, which provide facilitated electron transfer. The C$_S$ was slowly decreased with increasing the scan rate. As regards, proton transfer process is slow, higher scan rate leads to saturation of the protons in the electrolyte/electrode interface during the redox process. This mainly results that increase of ionic resistivity leading to drop in the capacitance of the electrodes.

Galvanostatic charge-discharge cycling between 0 and 1 V of samples in 0.5 mol L^{-1} Na$_2$SO$_4$ and different current densities (1-8 A g^{-1}) were shown in Figure 5. All curves exhibited an almost equilateral triangle shape indicating the good efficiency of the charge-discharge process. There is a linear relation between potential and time during charging and discharging processes, which is another reason for capacitance behavior of a material in addition to exhibiting rectangular voltammograms. The IR drop (cell potential drop) is attributed to the internal resistance of the electrode associated with electrical connection resistance, bulk solution resistance, and resistance of ion migration in electrode materials. It can be seen that the IR drop in the films prepared with pulsed current melthod is obviously lower than others (Figures 5b, 5d, 5f). It can be seen that
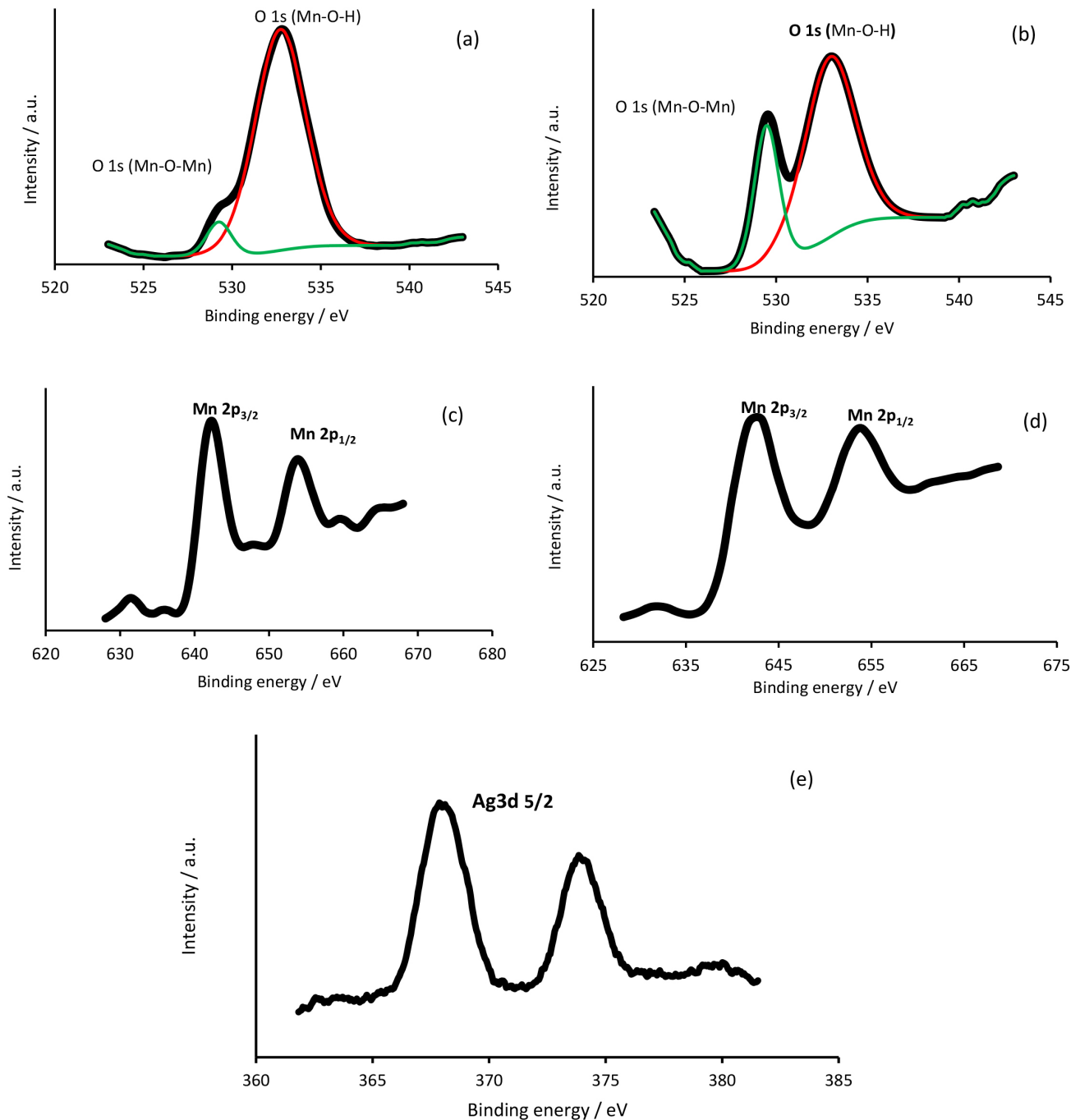
Figure 3. Smoothed XPS spectra of samples (a) O1s spectra for MCA-g; (b) O1s spectra for MCA-p; (c) Mn2p spectra for MCA-g; (d) Mn2p spectra for MCA-p; (e) Ag3d for MCA-p.

MCA-g and MCA-p have the highest capacitance among all the examined electrodes and shows good rate capability (Figures 5e and 5f). Specific capacitance was decreased with increasing the current density (Figure 6). Better capacitance behavior and lower IR drop in the MCA-g and MCA-p samples may be attributed to the fact that the presence of CTAB and Ag can provide a conductivity for the MnO_2 in electron transfer process. Herein, the MCA-g and MCA-p shows higher and better capacitance behavior than

the sample in which MnO_2 was the electrode. The CC was investigated galvanostatically at various current densities (1-8 A g^{-1}). C_S and ED of all electrodes at current density of 1 A g^{-1} are summarized in Table 2. Specific capacitances were measured to be 269, 315, 435, 442, 480 and 508 F g^{-1} at current density of 1 A g^{-1} for M-g, M-p, MC-g, MC-p, MCA-g and MCA-p, respectively.

For more investigating, alternating current (AC) impedance measurements were performed (Figure 7). It
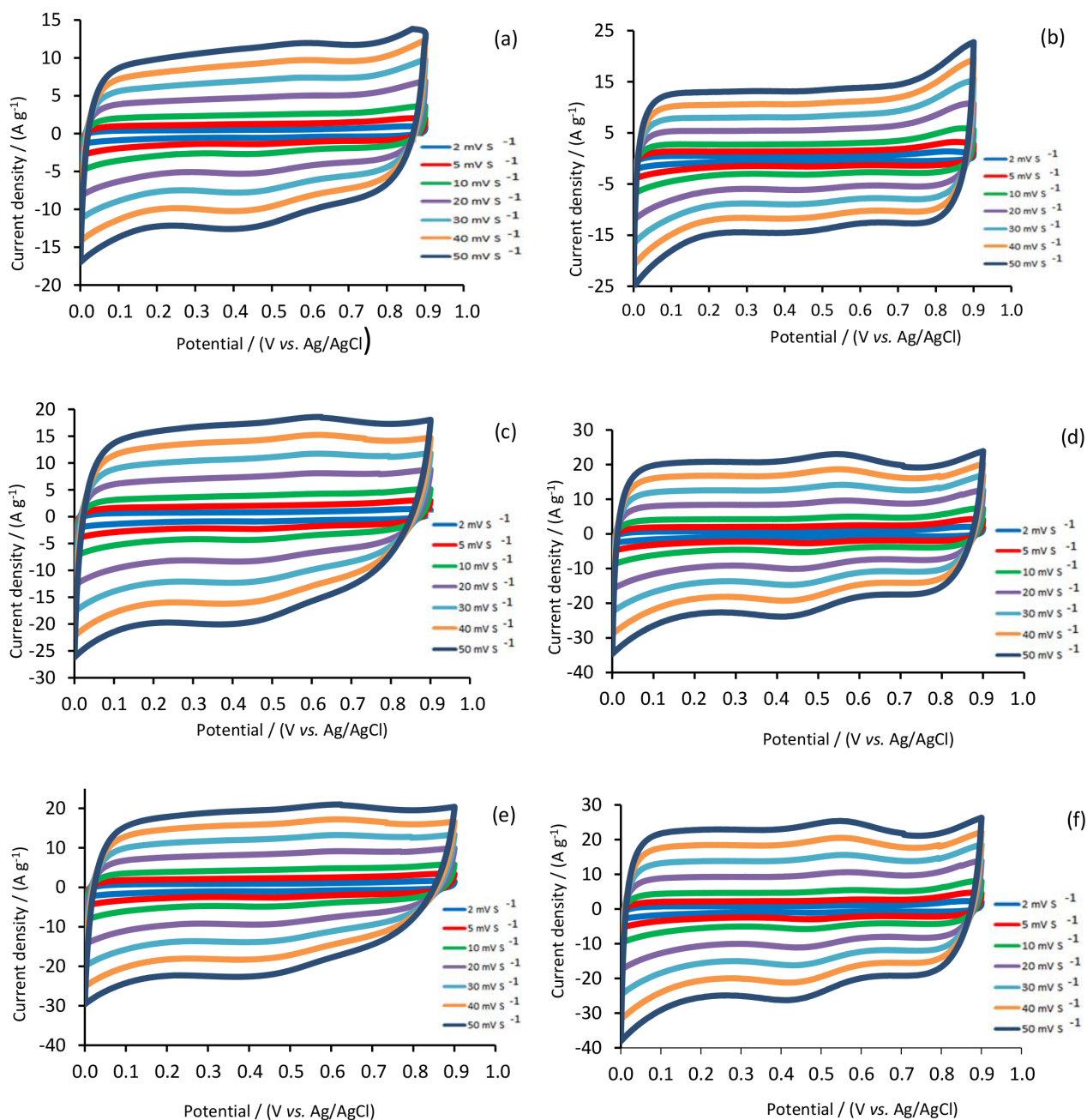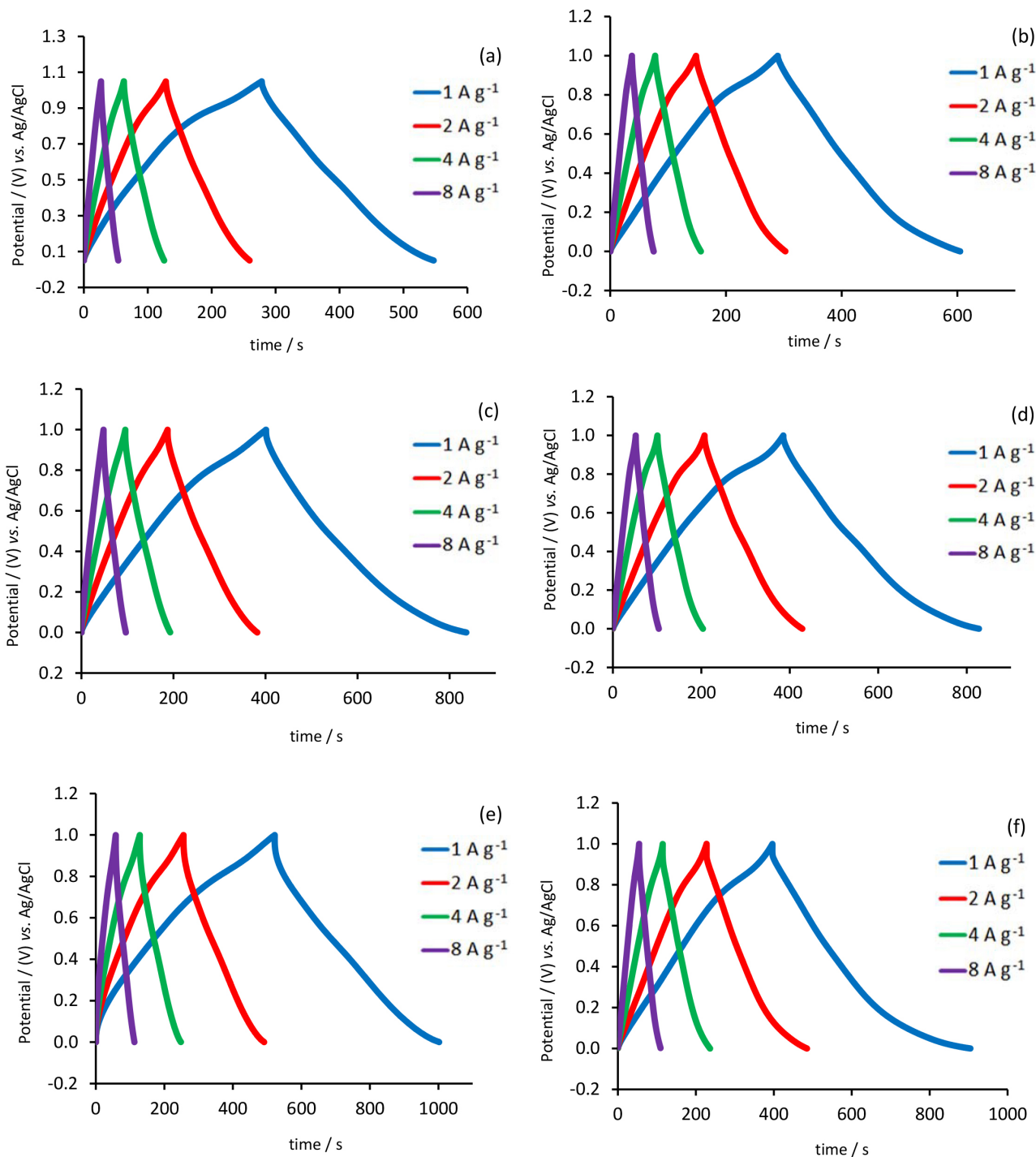
Figure 4. CV curves of (a) M-g; (b) M-p; (c) MC-g; (d) MC-p; (e) MCA-g; (f) MCA-p at various scan rate (2-50 mV s^{-1}) in aqueous 0.5 mol L^{-1} Na$_2$SO$_4$.

should be noted that Nyquist plot of an ideal supercapacitor is comprised of a vertical line, while appearing a semicircle at high frequency region is indicative of interfacial charge transfer resistance. It demonstrates a semicircle in high-frequency and a linear curve in the low-frequency region. The semicircle in the high-frequency region is related to reaction kinetics at the electrode and electrolyte interfaces. Linear curve at the low-frequency region can be attributed to diffusion controlled process in the electrolyte. Based on Nyquist plots (Figure 7), faradic charge transfer resistance (R$_{ct}$) of M-g, M-p, MC-g, MC-p, MCA-g and

MCA-p obtained were 52.75, 26.06, 32.4, 13.1, 17.1 and 6.28 Ω cm^{-2}, respectively. These results show faster charge transfer rate for films that were electrodeposited by pulsed current. As it can be seen, the Ag doped electrodes have got significantly lower charge-transfer resistance values in comparison with other samples which is attributed to the improved electrical conductivity in these samples, due to contribution of highly-conductive Ag components. R$_{ct}$ decreases after modification with Ag and CTAB. Slope of linear section in high frequency in MCA-p becomes close to nearly vertical line, which indicate a nearly pure

Figure 5. Galvanostatic charge-discharge curves of (a) M-g; (b) M-p; (c) MC-g; (d) MC-p; (e) MCA-g; (f) MCA-p at various current density (1-8 A g^{-1}) in aqueous 0.5 mol L^{-1} Na$_2$SO$_4$.

capacitive behavior. The near vertical line proves that electrostatic charge-discharge process for MCA-p in Na$_2$SO$_4$ is strongly fast.

The stability of the MnO$_2$ based electrodes were also investigated by continuous charge-discharge measurements over 1000 cycles at a current density 1 A g^{-1}, as shown in Figure 8. As can be seen, the capacitance for MCA-p

gradually decreases to 433 F g^{-1} after 1000 cycles corresponding to a capacitance loss of 7.5%. Based on the cycling performance (Figure 8), the capacitance loss of M-g, M-p, MC-g, MC-p, MCA-g and MCA-p obtained is 6.6, 2.3, 2.4, 7.5, 7.5 and 7.5%, respectively. These observations demonstrate cycling performance of MnO$_2$ based electrodes.
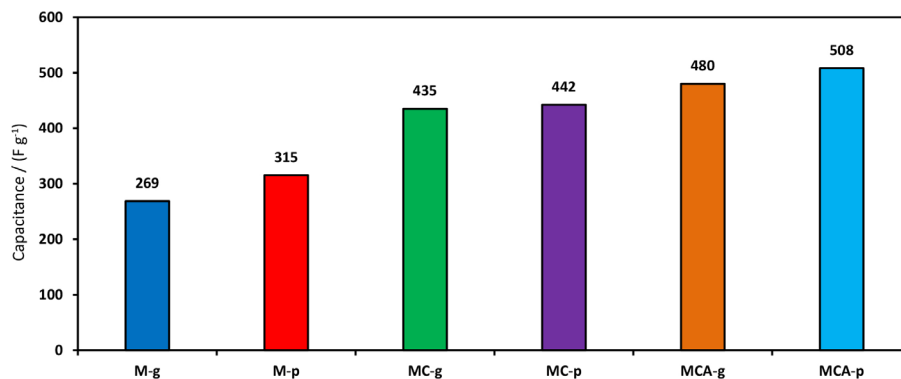
Figure 6. The charge-discharge specific capacitance of the samples at a 1 and 8 A g^{-1}.

Table 2. Values of specific capacitance and energy density at current density of 1 A g^{-1} for all samples

Sample	Specific capacitance / (F g^{-1})	Energy density / (Wh kg^{-1})
M-g	269	37
MC-g	435	60
MCA-g	480	67
M-p	315	44
MC-p	442	61
MCA-p	508	71

Conclusions

MnO$_2$-based electrodes in presence Ag and CTAB were successfully synthesized by galvanostatic and pulse deposition techniques, and applied as supercapacitor electrode active material. Surface morphology of the MnO$_2$ electrode is more compact when we used pulse deposition techniques. The MCA-p electrode exhibited good electrochemical performance including high specific capacitance (508 F g^{-1} at 1 A g^{-1}), high energy density and
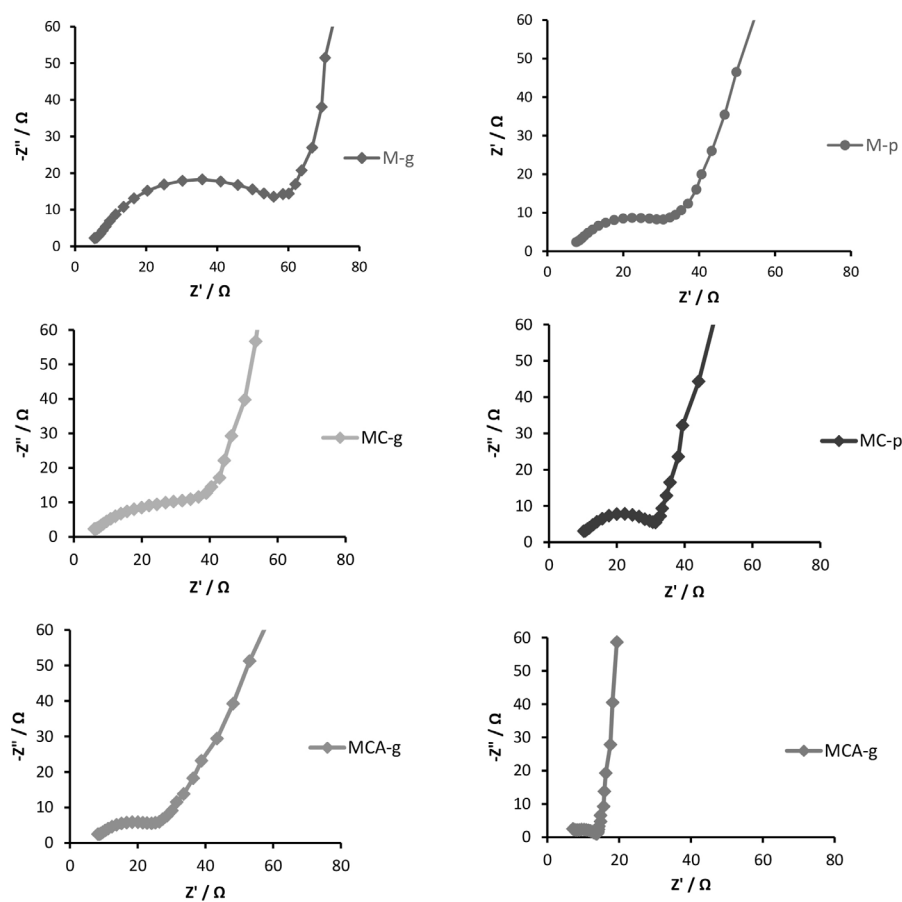
Figure 7. Nyquist plots of all MnO$_2$ based electrodes obtained at open circuit potential over the frequency range 0.01 to 100 kHz.
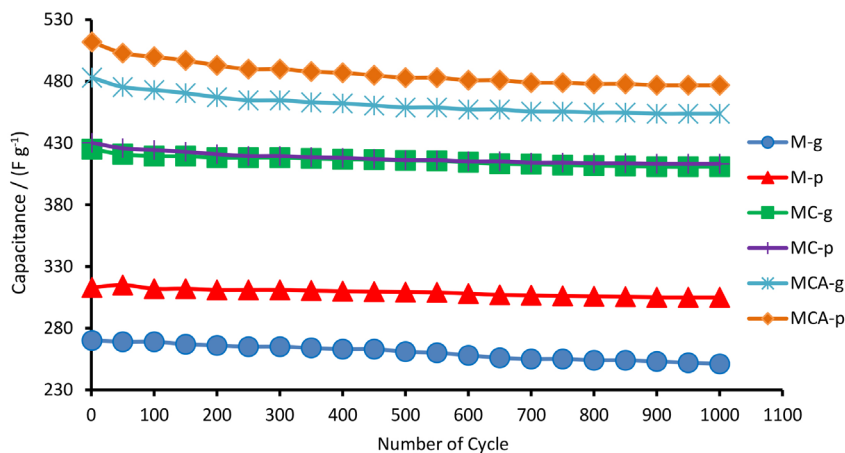
Figure 8. Cycling performance of the MnO$_2$ electrodes at a current density 1 A g^{-1}.

excellent cycling stability. This good electrochemical performance related to surface morphology, CTAB addition and Ag doping. Moreover, Ag doped electrodes have significantly lower charge-transfer resistance values in comparison with other electrodes which have attributed to developed electrical conductivity.

Supplementary Information

Supplementary information (the specific capacitances of all MnO$_2$ based films at different scan rates calculated) is available free of charge at http://jbcs.sbq.org.br as PDF file.

Acknowledgments

References

1. Winter, M.; Brodd, R. J.; *Chem. Rev.* **2004**, *104*, 4245.

2. Sharma, P.; Bhatti, T.; *Energy Convers. Manage.* **2010**, *51*, 2901.

3. Zhi, M.; Xiang, C.; Li, J.; Li, M.; Wu, N.; *Nanoscale* **2013**, *5*, 72.

4. Anwar, A. W.; Majeed, A.; Iqbal, N.; Ullah, W.; Shuaib, A.; Ilyas, U.; Bibi, F.; Rafique, H. M.; *J. Mater. Sci. Technol.* **2015**, *31*, 699.

5. Devadas, A.; Baranton, S.; Napporn, T. W.; Coutanceau, C.; *J. Power Sources* **2011**, *196*, 4044.

6. Mondal, S. K.; Munichandraiah, N.; *J. Power Sources* **2008**, *175*, 657.

7. Zhi, J.; Deng, S.; Zhang, Y.; Wang, Y.; Hu, A.; *J. Mater. Chem. A* **2013**, *1*, 3171.

8. Yeager, M. P.; Su, D.; Marinković, N. S.; Teng, X.; *J. Electrochem. Soc.* **2012**, *159*, A1598.

9. Moosavifard, S. E.; Shamsi, J.; Fani, S.; Kadkhodazade, S.; *RSC Adv.* **2014**, *4*, 52555.

10. Xie, K.; Li, J.; Lai, Y.; Lu, W.; Zhang, Z. A.; Liu, Y.; Zhou, L.; Huang, H.; *Electrochem. Commun.* **2011**, *13*, 657.

11. Selvan, R. K.; Perelshtein, I.; Perkas, N.; Gedanken, A.; *J. Phys. Chem. C* **2008**, *112*, 1825.

12. Huang, H.; Wang, X.; *Nanoscale* **2011**, *3*, 3185.

13. Yu, G.; Hu, L.; Liu, N.; Wang, H.; Vosgueritchian, M.; Yang, Y.; Cui, Y.; Bao, Z.; *Nano Lett.* **2011**, *11*, 4438.

14. Duay, J.; Sherrill, S. A.; Gui, Z.; Gillette, E.; Lee, S. B.; *ACS Nano* **2013**, *7*, 1200.

15. Ma, W.; Chen, S.; Yang, S.; Chen, W.; Cheng, Y.; Guo, Y.; Peng, S.; Ramakrishna, S.; Zhu, M.; *J. Power Sources* **2016**, *306*, 481.

16. Wan, C.; Cheng, M.; Zhang, Q.; Jia, N.; *Powder Technol.* **2013**, *235*, 706.

17. Dubal, D.; Kim, W.; Lokhande, C.; *J. Phys. Chem. Solids* **2012**, *73*, 18.

18. Gupta, V.; Gupta, S.; Miura, N.; *J. Power Sources* **2008**, *175*, 680.

19. Prasad, K. R.; Miura, N.; *J. Power Sources* **2004**, *135*, 354.

20. Fang, Y.; Liu, J.; Yu, D. J.; Wicksted, J. P.; Kalkan, K.; Topal, C. O.; Flanders, B. N.; Wu, J.; Li, J.; *J. Power Sources* **2010**, *195*, 674.

21. Sharma, R.; Rastogi, A.; Desu, S.; *Electrochem. Commun.* **2008**, *10*, 268.

22. Davies, A.; Audette, P.; Farrow, B.; Hassan, F.; Chen, Z.; Choi, J.-Y.; Yu, A.; *J. Phys. Chem. C* **2011**, *115*, 17612.

23. Hu, C. C.; Tsou, T. W.; *Electrochim. Acta* **2002**, *47*, 3523.

24. Chang, J. K.; Tsai, W. T.; Chen, P. Y.; Huang, C. H.; Yeh, F. H.; Sun, I. W.; *Electrochem. Solid-State Lett.* **2007**, *10*, A9.

25. Shinomiya, T.; Gupta, V.; Miura, N.; *Electrochim. Acta* **2006**, *51*, 4412.

26. Zhao, T.; Jiang, H.; Ma, J.; *J. Power Sources* **2011**, *196*, 860.

27. Subramania, A.; Devi, S. L.; *Polym. Adv. Technol.* **2008**, *19*, 725.

28. Zhang, K.; Mao, L.; Zhang, L. L.; Chan, H. S. O.; Zhao, X. S.; Wu, J.; *J. Mater. Chem.* **2011**, *21*, 7302.

29. Mao, L.; Zhang, K.; Chan, H. S. O.; Wu, J.; *J. Mater. Chem.* **2012**, *22*, 80.

30. Senthilkumar, B.; Thenamirtham, P.; Selvan, R. K.; *Appl. Surf. Sci.* **2011**, *257*, 9063.

31. Wu, M.-S.; Wang, M.-J.; *Chem. Commun.* **2010**, *46*, 6968.

32. Ahn, H.-J.; Sung, Y.-E.; Kim, W. B.; Seong, T.-Y.; *Electrochem. Solid-State Lett.* **2008**, *11*, A112.

33. Huang, J.; Wu, H.; Cao, D.; Wang, G.; *Electrochim. Acta* **2012**, *75*, 208.

34. Adelkhani, H.; Ghaemi, M.; *J. Alloys Compd.* **2010**, *493*, 175.

35. Ghaemi, M.; Khosravi-Fard, L.; Neshati; *J. Power Sources* **2005**, *141*, 340.

36. Hedborg, E.; Winquist, F.; Lundström, I.; *Thin Solid Films* **1994**, *240*, 147.

37. Savitzky, A.; Golay, M. J.; *Anal. Chem.* **1964**, *36*, 1627.

38. Kaspar, T. C.; Droubay, T.; Chambers, S. A.; Bagus, P. S.; *J. Phys. Chem.* **2010**, *114*, 21562.

39. Hermas, A. A.; *Corros. Sci.* **2008**, *50*, 2498.

40. Wu, M.-S.; Lee, J.-T.; Wang, Y.-Y.; Wan, C.-C.; *J. Phys. Chem. B* **2004**, *108*, 16331.